RSC Advances

ROYAL SOCIETY OF CHEMISTRY

www.rsc.org/advances

Synthesis, Characterisation and Enhanced Electrochemical Performance of Nanostructured Na_2FePO_4F for Sodium Batteries

Markas Law,[a] Vishwanathan Ramar,[a] and Palani Balaya*[a]

Abstract

Nanostructured pure Na_2FePO_4F was synthesised by a soft template method, followed by high-energy ball milling (HEBM) process and post-heat treatment. Physical and electrochemical properties of this sample were compared with as-prepared (pristine) sample. FESEM images recorded on the ball milled samples showed that the particles were of spherical morphology, with particle size centred around 100 nm. BET analysis illustrated a correlation between the surface area of the material with the electrochemical performance. Rietveld refinement of XRD patterns of the pristine and the HEBM samples together with the obtained reliability factor values demonstrated lower percentage of antisite disorder in HEBM sample. Compared to the pristine sample, which delivered an initial discharge capacity of only 87 mAh g^{-1}, the HEBM sample showed an impressive storage capacity of 116 mAh g^{-1} at 0.1 C. Furthermore, at 1 C after 200 cycles, the ball milled sample displayed stable cyclability, retaining almost 80% of its initial discharge capacity, with an average coulombic efficiency of 99.4%. The improved sodium storage performance as compared to the pristine sample is discussed in terms of the reduced antisite disorder and associated sodium ion diffusion.

Introduction

Sodium-ion battery, involving intercalation-deintercalation of sodium ions in its active materials using non-aqueous sodium-based electrolytes was explored in the mid-1980s.[1, 2] Since then it did not attract much attention for applications such as computers or mobile phones due to their inherent lower energy density compared to lithium-ion battery. However with the emergence of renewable energy options for stationary applications such as micro-grids, solar energy systems, etc., where the footprint is not a serious concern, sodium-ion battery has undergone resurgence in the last few years with quite a number of new materials and approaches to enhance its performance.

A great range of cathode materials are being investigated in recent times for sodium-ion battery, each exhibiting its own advantage and disadvantage.[3] In particular, sodium fluorophosphate-based compounds have been studied and tested as a potential cathode for sodium-ion battery due to its relatively high voltage and stable long-term cycling. Recent publications have shown that this material exhibits comparable electrochemical behaviour as its lithium-based counterpart.[4, 5]

Amongst the possible fluorophosphate materials, sodium iron and/or manganese fluorophosphates appear the most in the literature. Both the compounds have different crystal structure, where the iron-phase possesses a two-dimensional (2D) layered structure with the space group of *Pbcn*, while the manganese-phase takes up a three-dimensional tunnel structure with space group of $P2_1/n$.[6, 7] Recent studies have focused on the iron compound because of its better electrochemical performance, while the manganese compound is less described due to poor electrochemical properties.

The literature on Na_2FePO_4F mainly focuses on the electrochemical storage performance. The first report on Li/Na_2FePO_4F was published in 2007 by Ellis et al.[8] demonstrating the possibility of desodiation via a slopping solid-solution curve during the charging process. However, sodium storage of this compound using electrochemical studies was not shown in this study. Two years later, Recham et al.[9] reported the first study of sodium storage in Na_2FePO_4F prepared via ionothermal synthesis. Their cathode delivered a capacity of 120 mAh g^{-1}. In 2011, Wu et al.[6] prepared Na_2FePO_4F via a sol-gel synthesis and performed galvanostatic charge/discharge cycling in a lithium cell at elevated temperature of 60°C. They thus reported lithium storage with a high reversible capacity of 182 mAh g^{-1}, which corresponds to 1.46 electron exchange per unit formula. They have successfully shown that more than one electron exchange is feasible, involving the Fe^{3+}/Fe^{4+} redox couple at high temperature. Kawabe et al.[10] prepared Na_2FePO_4F by a solid-state route using ascorbic acid as the carbon source and demonstrated that the inclusion of an in-situ carbon source greatly enhances the electrochemical performance. Recently, Langrock et al.[11] synthesised a carbon-coated hollow Na_2FePO_4F using ultrasonic spray pyrolysis. The spherical particle morphology of this hollow Na_2FePO_4F had an average size of 500 nm with a wall thickness of 80 nm and managed to store sodium with an initial discharge capacity of 90 mAh g^{-1}, retaining 90% capacity after 100 cycles at 0.1 C.

Here, we report electrochemical properties of the nanostructured Na_2FePO_4F synthesised by a soft template method, followed by high-energy ball milling (HEBM) process and post-heat treatment. This HEBM sample shows excellent sodium storage performance as compared to pristine material (involving no HEBM process) with an initial discharge capacity of 116 mAh g^{-1} at 0.1 C. The cause for this impressive sodium storage performance is elucidated in terms of its particle size, surface area, enhanced diffusion kinetics, and relatively low antisite disorder concentration.

Experimental

Material synthesis

Nanostructured pure Na_2FePO_4F was synthesised via a soft template method using NaF as the only sodium precursor. Typically, 1.0 mmol of cationic surfactant, hexadecyltrimethylammonium bromide (CTAB) ($CH_3(CH_2)_{15}N(Br)(CH_3)_3$, Sigma-Aldrich, purity 96%) was dissolved in a mixture of absolute ethanol and milli-Q water in the volume ratio of 6:5. The solution was stirred for 60 min, to trigger the formation of micelles. This was then followed by addition of anhydrous iron(II)acetate ($Fe(CH_3COO)_2$, Strem Chemicals, 97%), sodium fluoride (NaF, Merck, >99.5%) and ammonium dihydrogen phosphate ($NH_4H_2PO_4$, Alfa Aesar, 98%) in

the molar ratio of 1:2:1, respectively. The obtained brown solution was further stirred for another 24 h at room temperature to homogeneously mix the precursors. The ethanol-water solvent was removed using a rotary evaporator (Heidolph Hei-VAP Precision ML/G3). The obtained precipitate was grounded and calcined in a tubular furnace (MTI Corporation, USA) at 550°C for 6 h under argon atmosphere. The as-prepared product was then ball milled with Super P carbon black (Alfa Aesar, >99%) using a planetary milling machine (Fritsch Planetary Micro Mill PULVERISETTE 7 premium line) at 500 rpm for 4 h with the weight ratio of sample:balls = 1:40.[12] The obtained ball milled sample was then post-heat treated in a tubular furnace at 550°C for 3 h under argon atmosphere to alleviate the strain build-up during the high energy ball milling process.[13]

Material characterisation

Powder X-ray diffraction (PXRD) was performed on both the pristine and ball milled samples with a Bruker D2 PHASER desktop X-ray diffractometer using Cu-Kα radiation operated at 40 kV and 30 mA from a 2θ angle of 10° to 60°. Rietveld refinement was performed on the obtained PXRD patterns using TOPAS version 3 software with a Chebyshev polynomial function.

Morphological characteristics of the samples were observed using a field-emission scanning electron microscope (FESEM; JEOL JSM-7000F) operated at 15 kV and 20 mA. Prior to the FESEM observation, the samples were coated with a thin platinum layer using an auto fine coater (JEOL JFC-1600) to increase the surface conductivity.

Thermogravimetric analysis (TGA) was performed using a simultaneous DTA-TGA system (TA Instruments SDT-2960) to study the decomposition and reaction of the precursor and to determine the carbon content of the samples. For the former analysis, the precursor was heated under nitrogen at a heating rate of 5°C min.$^{-1}$ starting from room temperature to 700°C. For the latter, the experiment was performed in air at a heating rate of 5°C min^{-1} starting from room temperature to 600°C. The experiment was performed on 12-15 mg of samples.

Composition of the elements present (Na, Fe and P) in both the samples was estimated by elemental analysis using the Dual-view Optima 5300 DV ICP-OES system. Sample was digested with HNO_3/HCl and top up to 10 ml with H_2O. Precipitate was observed prior to analysis.

Nitrogen-physisorption characterisation was recorded at 77 K using a Nova 2200e surface area analyser (Quantachrome, USA). Prior to the experiment, the samples were degassed in vacuum at 110°C for 16 h. The Brunauer-Emmett-Teller (BET) specific surface area was determined from nitrogen adsorption isotherm in the relative pressure range, P/P_0 of 0.05-0.3. The total pore volume was estimated from the amount of nitrogen adsorbed at a relative pressure of ~0.99.

X-ray photoelectron spectroscopy (XPS) analysis was performed with a Kratos AXIS Ultra^{DLD} (Kratos Analytical Ltd) at a base pressure of 1×10^{-9} Torr and a working pressure of 1×10^{-9} Torr using a mono Al-Kα radiation operated at 15 kV and 5 mA. The XPS spectrum was fitted using the XPSPEAK software version 4.1. A Shirley-type background was subtracted from the recorded spectrum. The derived binding energies (BE) are accurate to ±0.1 eV.

Electrochemical characterization

Electrochemical measurements of the Na_2FePO_4F electrode material were carried out on 2016 type coin- cells. The electrode was prepared by mixing the active material, Super P carbon black and binder in the weight ratio 70:20:10, The binder consists of a mixture of polyvinylidene fluoride (PVDF; Kynar 2801) and N-methyl-2-pyrrolidone (NMP; Merck) in the weight ratio 1:10. The mixture was made into slurry and coated on an etched aluminium foil of 0.015 mm thickness (Shenzhen Vanlead, China) using doctor blade technique. The pasted electrode was dried in a vacuum oven (Memmert, Germany) at 110°C for 6 h. The dried electrode was then pressed using a desktop roller-press (Hohsen Corporation, Japan) with a pressure of 37 psi to ensure intimate contact between the electrode material and the current collector. The pressed electrode was punched into circular discs and dried again at 110°C for 6 h in a vacuum antechamber to remove any trace of moistures. The geometrical area of the electrode is 2.01 cm^2 for 2016 coin-type cells, and 0.95 cm^2 for a Swagelok-type electrode. The typical active material loading on the electrode is 1.4-1.5 mg cm^{-2}.

The coin-cells were assembled in an argon-filled glove box (MBraun, Germany) with metallic sodium as the counter electrode and glass microfiber filters (Whatman; Grade GF/C) as the separator. A split flat three-electrode setup (MTI Corporation) was used to assemble three-electrode electrochemical cell for electrochemical impedance spectroscopy (EIS) measurement over the frequency range of 10 mHz to 1 MHz, the counter and reference electrodes used were metallic sodium disc and ring, respectively, with Na_2FePO_4F as the working electrode. The electrolyte used was 1 M $NaClO_4$ in ethylene carbonate (EC; Sigma-Aldrich)-propylene carbonate (PC; Sigma-Aldrich) (1:1 volume ratio). The assembled coin-cell (a two-electrode setup) was galvanostatically charged and discharged between 2.0-4.0 V at room temperature using a battery testing station (Arbin Instruments BT-2000). Cyclic voltammetry (CV) experiment was carried out on coin-cells between 2.0-4.0 V, at a scan rate of 0.05 mV s^{-1} at room temperature. Both the electrochemical studies (EIS and CV) were carried out using a VMP3 tester (BioLogic Science Instruments, France). The obtained experimental data were analysed using EC-Lab version 10.19.

Results and discussion

Structural and morphological analysis

Fig. 1 shows the thermogravimetric analysis (TGA) curve of the precursor obtained after rotary evaporation. It is observed that the total weight loss is about 40 %, and the weight loss stops at a temperature beyond 540°C.

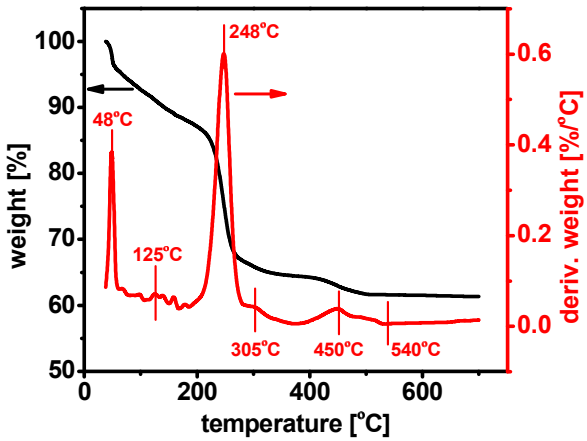

Fig. 1 TGA curve of the precursors obtained at a heating rate of 5°C min^{-1} from room temperature to 700°C.

The TGA curve reveals four main stages of weight loss. Starting from 30°C to 125°C, the precursor experiences a loss of about 10 wt.%, which is mainly attributed to the loss of crystallisation water.[14] From 125°C to 248°C, the precursor losses about 16 wt.% of its weight due to the thermal decomposition of CTAB, $Fe(CH_3COO)_2$ and $NH_4H_2PO_4$.[14] Further weight loss of ~9 % at a temperature range of 248°C to 305°C is ascribed to the continuous thermal decomposition of CTAB, $Fe(CH_3COO)_2$ and $NH_4H_2PO_4$. The continuous weight loss of about 5 % in the temperature range of 305°C to 540°C is attributed to the thermal decomposition of remaining organics.[14] Further heating at temperatures beyond 540°C only improves the crystallinity of the samples.

The carbon content of the pristine as well as HEBM samples was determined by TGA analysis (**Fig. S1**). The total carbon content of the pristine sample was determined to be 5 wt.%. The total carbon content for the HEBM sample was measured to be around 25 wt.%, which originated from the 5% *in-situ* and 20% *ex-situ* Super P carbon.

Table 1 Elemental (Na, Fe and P) composition in the pristine and HEBM samples.

Material	Na content	Fe content	P content
Pristine	18.92 wt%	22.93 wt%	12.75 wt%
	2.00 mol	1.00 mol	1.00 mol
HEBM	12.48 wt%	15.14 wt%	8.42 wt%
	2.00 mol	1.00 mol	1.00 mol

a Footnote text

Table 1 provides the elemental composition in the pristine and HEBM samples obtained from ICP elemental analysis. It is clearly seen that both the samples have a Na:Fe:P stoichiometric molar ratio of 2:1:1, corresponding to the molecular formula of Na_2FePO_4F.

The PXRD patterns shown in **Fig. 2** confirm single-phase formation of Na_2FePO_4F without any observable impurity phases irrespective of the synthesis conditions. The lattice parameters of these samples are shown in **Table 2**, which are in good agreement with the literature[6, 8-10, 15, 16].

Table 2 also presents changes in the lattice parameters and the unit cell volume of these samples compared to the standard Na_2FePO_4F. The changes in the unit cell volume of these samples can be due to the presence of antisite disorder in the respective samples[17] (which will be shown later). Substitution of a bigger ion into sites which belong to a smaller ion (e.g. Na^+ into Fe^{2+} sites) is known to increase the lattice parameters, ultimately increasing the cell volume. Under this line, a small amount of antisite disorder is present in the HEBM sample, the unit cell volume increases only by 0.06% with respect to the standard sample reported in literature. With an increase in antisite disorder concentration as can be seen in the pristine sample, the unit cell volume experience a greater increase of 0.15%. Substitution of a bigger ion into sites which belong to a smaller ion (e.g. Fe^{2+} into Na^+ sites) is known to increase the lattice parameters, ultimately increasing the cell volume.[18]

Although both the pristine and HEBM samples exhibit pure phase of Na_2FePO_4F, the effect of ball milling can significantly alters the particle size and morphology.[19] **Fig. 3** depicts the FESEM images of the pristine and the HEBM samples, respectively. As shown in **Fig. 3a**, the particle size of pristine sample falls in the range of 200-300 nm. In contrast, **Fig. 3b** shows noticeably smaller, more uniform particle morphology for HEBM sample, with a uniform crystallite size distribution centred around 100 nm.

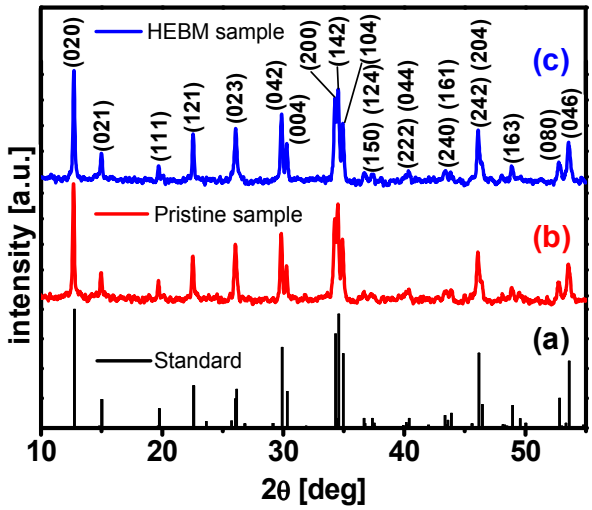

Fig. 2 PXRD patterns of (a) standard Na2FePO4F, (b) Na2FePO4F calcined at 550°C for 6h (pristine sample), and (c) Na2FePO4F calcined and ball milled at 500 rpm for 4 h and heat-treated at 550°C for 3h (HEBM sample).

Table 2 Lattice parameters and the cell volume of pristine and ball milled Na_2FePO_4F samples obtained by Rietveld analysis.

Material	*a* (Å)	*b* (Å)	*c* (Å)	*V* (Å^3)	ΔV (%)
Standard Na_2FePO_4F	5.220000	13.85400	11.77920	851.8500	-
Pristine	5.22468(29)	13.85789(92)	11.78281(92)	853.111(99)	0.15
HEBM	5.22377(30)	13.8362(10)	11.7930(10)	852.36(11)	0.06

a Footnote text

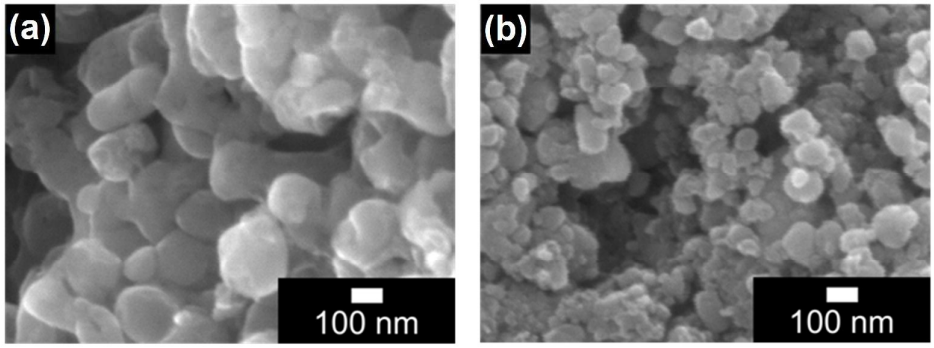

Fig. 3 FESEM images of (a) pristine; and (b) HEBM samples.

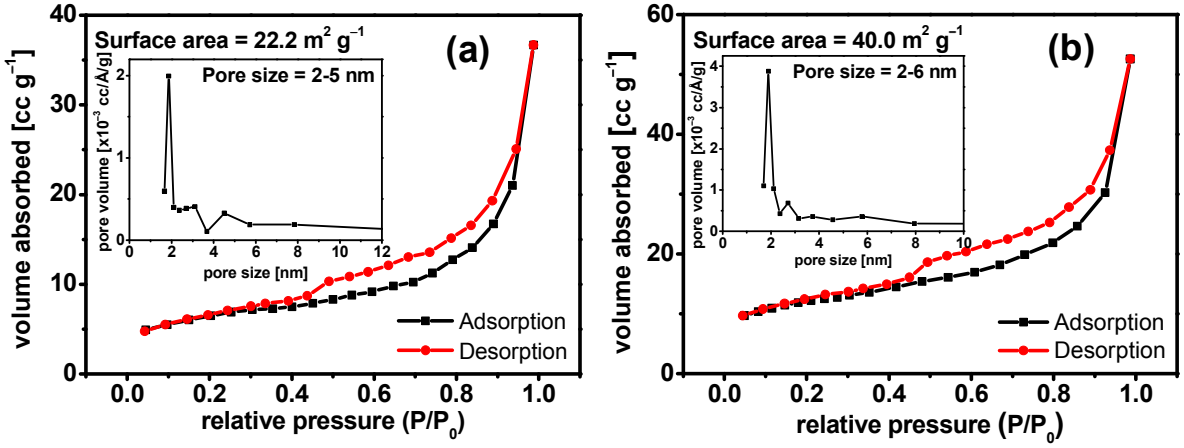

Fig. 4 Nitrogen physisorption isotherms of (a) pristine; and (b) HEBM samples with inset showing BJH pore size distribution.

Fig. 4 shows the nitrogen-physisorption characteristics and their respective BJH pore size distributions for all the samples reported here. All samples feature a well-defined hysteresis loop, which is attributed to a Type-IV isotherm associated with a

mesoporous nature.[20] BET surface area of the pristine sample is measured to be 22.2 m^2 g^{-1}, with a pore size distribution between 2-5 nm (**Fig. 4a**). Interestingly, after 4 h ball milling, the BET surface area doubles to 40.0 m^2 g^{-1}, with a pore size distribution of 2-6 nm (**Fig. 4b**).

The study of Na-Fe antisite disorder

Na_2FePO_4F consists of pairs of face-sharing Fe octahedral, each coordinated to four oxygen and two fluorine ions, forming $Fe_2O_6F_3$ bioctahedral units (**Fig. 5a**). These units are connected by corner-sharing (via F site) to other pairs of Fe face-sharing octahedral along the *a*-axis (**Fig. 5b**). These connected chains of Fe octahedra are bonded through corner-sharing PO_4^{3-} tetrahedra along the *c*-axis (**Fig. 5c**). There are two crystallographically unique sites, Na1 and Na2 available for sodium ions (**Fig. 5**c).

Rietveld refinement was performed on the PXRD patterns of both the pristine and HEBM samples to obtain the positions of the ions, as well as the percentage of the antisites disorder and presented in **Fig. 6** and **Fig. 7**. Antisite disorder is a type of crystallographic defects where site-mixing of the cations occur, and is well-known in intercalation compounds.[21, 22]

The quality of the refinement was determined based on R_{wp}, R_p and R_{Bragg} values. According to Toby[23], the values of R_{wp} and R_p indicate how well the refined profile fits the measured profile. It can be seen that for both the samples, R_{wp} and R_p obtained is less than 3, which reflects a good refinement. The third reliability factor value, namely the R_{Bragg}, indicates how "correct" the modelled structure is with the measured profile[23]. It provides a valuable indication that the refined model is close to reproducing the crystallographic observations. In other words, R_{Bragg} presents an indication on how well the refined crystal structure agrees with the measured profile.

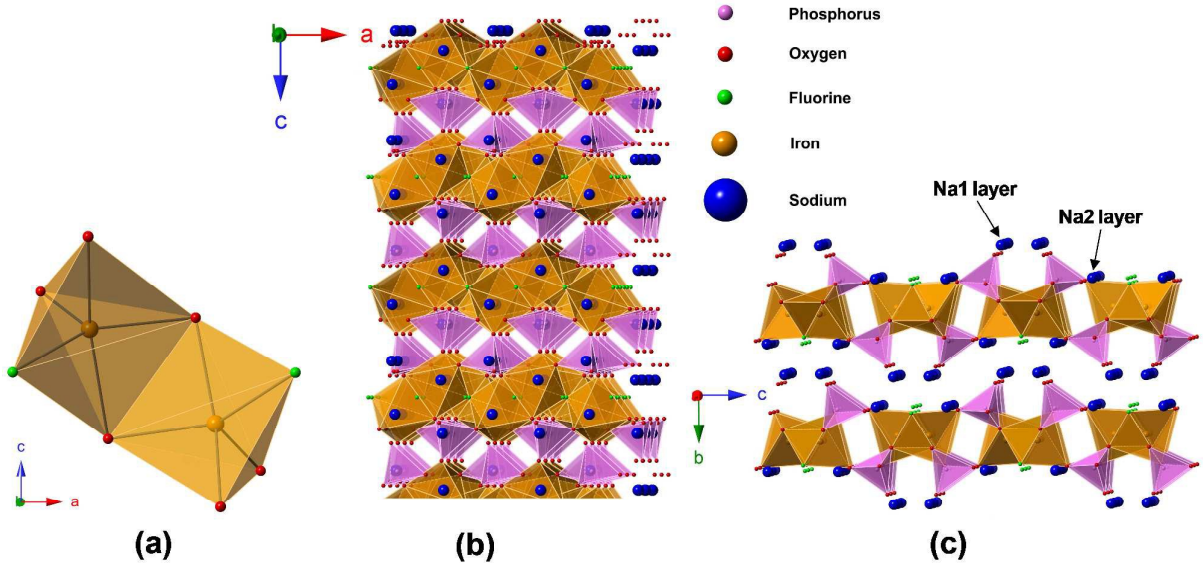

Fig. 5 Crystal structure of Na_2FePO_4F: (a) $Fe_2O_6F_3$ bioctahedral units; (b) view along [100]; and (c) along [010].

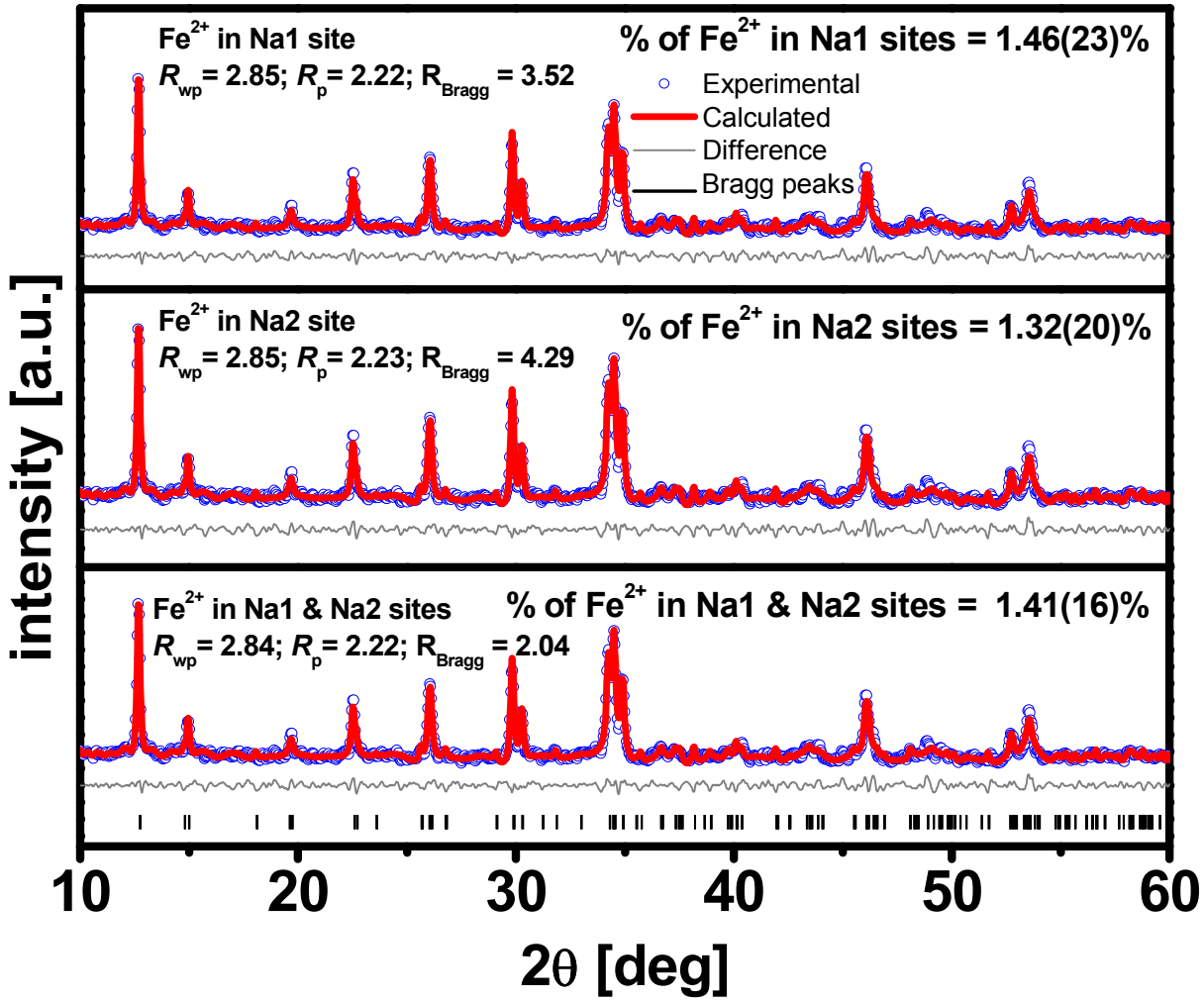

Fig. 6 Rietveld refinement profile of the pristine sample.

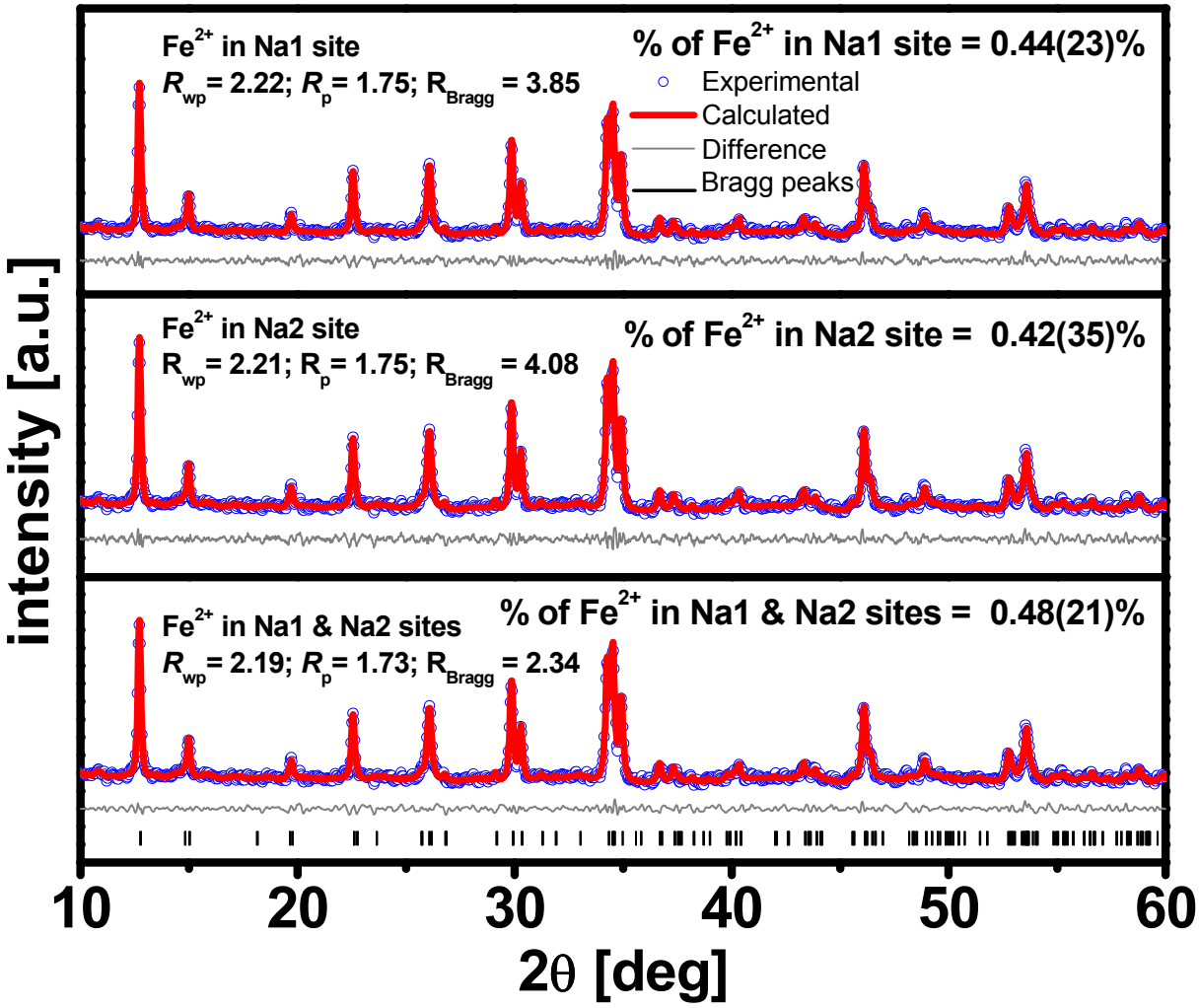

Fig. 7 Rietveld refinement profile of the HEBM sample.

To determine the site occupancies and the percentage of antisite disorder in the samples, four assumptions were made: (1) Fe^{2+} is occupying the Na1 site; (2) Fe^{2+} is occupying the Na2 site; (3) Fe^{2+} is simultaneously occupying both Na1 and Na2 sites; and (4) there is no antisite disorder. **Fig. 6** and **Fig. 7** show the Rietveld refinement pattern of the pristine and the HEBM samples, respectively, together with the obtained reliability factor values and the percentage of antisite disorder. A summary of the refinement results is shown in **Table 3**. The refined pattern for the fourth assumption for both the samples is shown in **Fig. S3.** Given that the R_{Bragg} value for the third assumption is better for both the samples, we conclude that Fe^{2+} is simultaneously occupying both the Na1 and Na2 sites.

Table 3 Summary of the results obtained from Rietveld refinement.

Sample	Fe^{2+} occupancy	R_{wp}	R_p	R_{Bragg}	% of antisite disorder
Pristine	Na1 site (Assumption 1)	2.85	2.22	3.52	1.46(23)
	Na2 site (Assumption 2)	2.85	2.23	4.29	1.32(20)
	Na1 and Na2 sites (Assumption 3)	2.84	2.22	2.04	1.41(16)
HEBM	Na1 site (Assumption 1)	2.22	1.75	3.85	0.44(23)
	Na2 site (Assumption 2)	2.21	1.75	4.08	0.42(35)
	Na1 and Na2 sites (Assumption 3)	2.19	1.73	2.34	0.48(21)

a Footnote text.

Antisite disorders possess critical problems for intercalation-based 1D olivine compounds such as $NaFePO_4$ because a single blocked path prevents continuous migration of ions.[16, 21, 24, 25] However in a 2D layered material such as Na_2FePO_4F, reduced antisite disorder causes great improvement in Na diffusion due to available channels in other orientations (along *a*-axis, *c*-axis or

across these axes).[16] From **Table 3**, the percentage of antisite disorder obtained for the HEBM sample is about 3 times less than the pristine sample. In this study, we believe that the relatively low percentage of antisite disorder demonstrated by the HEBM sample is due to the localised high temperature generated during the ball mill process. The local high temperature due to ball milling coupled with the post heat treatment at 550°C for 3 h in this 2D layered material with several possible channels for Na migration play an important role in the rearrangement of the cations in the crystal lattice, thus, bringing down the antisite disorder.[21, 26] Thus, ball milling along with the post heat treatment influences antisite disorder substantially in the 2D layered Na_2FePO_4F sample unlike 1D material like $NaFePO_4$ where the scope for rearrangement is rather limited.

Sodium storage performance

To understand how ball milling process influences the electrochemical performance of the Na_2FePO_4F samples, galvanostatic charge-discharge cycling was performed in a voltage window of 2.0-4.0 V. The sodium half-cell was cycled *vs.* sodium metal at a current rate of 0.1 C at room temperature. The HEBM sample exhibits two well-defined voltage plateaus corresponding to two reversible phase transformations of $Na_2Fe^{II}PO_4F \rightleftharpoons Na_{1.5}FePO_4F$ and $Na_{1.5}FePO_4F \rightleftharpoons NaFe^{III}PO_4F$.[11], centred at 2.92 V and 3.07 V, respectively (**Fig. 8**). This unique two-voltage plateau is characteristic to this material because of the difference in the Na^+ migration activation energies along the [100] and [001] directions.[16] The observed voltage plateaus are consistent with the reported literature on electrochemical performance of Na_2FePO_4F.[10, 11] The HEBM sample delivers a higher discharge capacity of 116 mAh g^{-1} close to theoretical capacity (124 mAh g^{-1}); while the pristine sample only managed to deliver a discharge capacity of 87 mAh g^{-1} at 0.1C.To further investigate the high rate storage performance of the HEBM sample, this material was tested at different C rates.

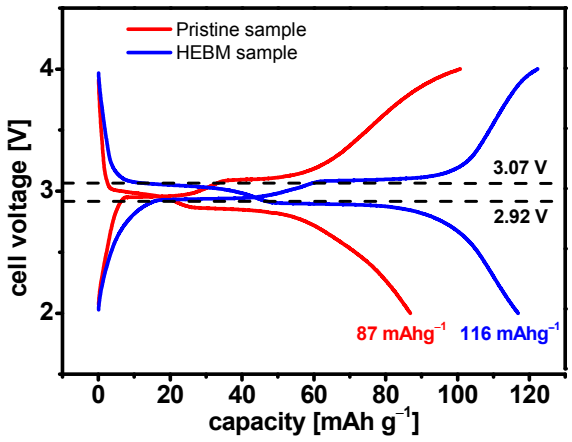

Fig. 8 Galvanostatic charge-discharge curves of the pristine and ball milled samples cycled at 0.1 C rate

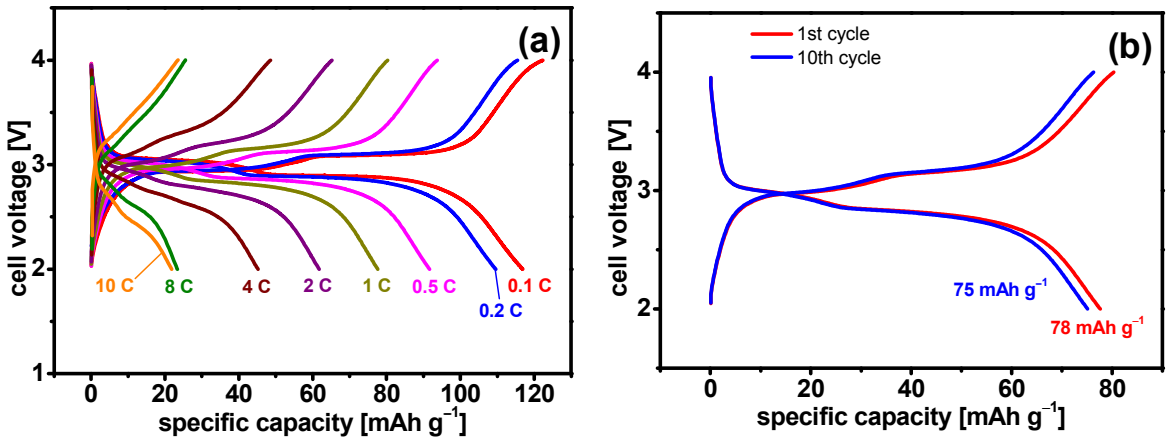

Fig. 9 (a) Galvanostatic charge-discharge curves of the HEBM sample cycled at different C rates; and (b) charge-discharge profile of the HEBM sample cycled at 1 C.

Fig. 9a depicts the galvanostatic charge-discharge curves of the HEBM sample tested at different C rates. At slow rates of 0.1 C, 0.2 C and 0.5 C, the HEBM sample is able to deliver a discharge capacity of 116, 109 and 92 mAh g^{-1}, respectively. At 1 C rate, the material exhibits a discharge capacity of 78 mAh g^{-1} on the 1st cycle, with the two distinct voltage plateaus, and retaining a discharge capacity of 75 mAh g^{-1} after the 10th cycle (**Fig. 9c**). At high C-rates of 2 C, 4 C, 8 C and 10 C, the sample is still capable of achieving moderate discharge capacity of 62, 47, 27 and 21 mAh g^{-1}, respectively. At these rates, the achieved capacity of this material is found to be relatively higher compared to the reported literature.[10, 11] The two voltage plateaus seen here during charging and discharging arises from the electrochemical activity of the working electrode itself due to difference in the Na ion diffusion kinetics along two directions (*a*- and *c*- axes) (**Fig. S2**), and not from the formation of a passivation film on the counter electrode, as suggested by Rudola, et al.[27]

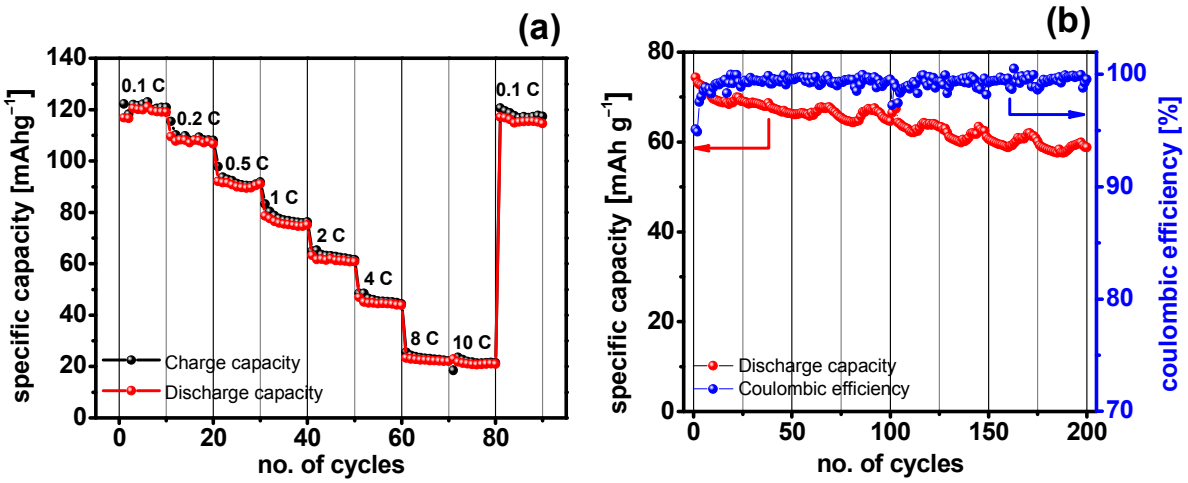

Fig. 10 (a) Rate performance; (b) long term cycling and coulombic efficiency at 1 C rate of the HEBM sample.

To further interpret the cycling behaviour of this material, a rate performance was conducted at various C rates, each cycled for 10 cycles. As shown in **Fig. 10a**, the HEBM sample demonstrates very stable charge-discharge capacities at different C-rates. After the test at 10 C, the cell was further tested at a slow rate of 0.1 C. The electrode exhibits excellent capacity recovery, regaining almost 100% of its initial capacity at 0.1 C. The long term cyclability and the coulombic efficiency of the HEBM sample are also evaluated at 1C. It displays remarkable cycling stability as shown in **Fig. 10b**, where a discharge capacity of close to 60 mAh g^{-1} is retained at the 200th cycle at room temperature, which translates to 80% capacity retention. The average coulombic efficiency throughout the 200th cycle is 99.4%.

Cyclic voltammetry

The pristine and HEBM samples were also characterised electrochemically by cyclic voltammetry (CV) to determine the activity of the iron redox couple. The cyclic voltammograms are shown in **Fig. 11**. Both the samples show a first anodic and cathodic peaks centred around 2.87 V and 2.98 V respectively, which correspond to the activity of Fe^{2+}/Fe^{3+} couple, attributed to the reversible phase transformations of $Na_2FePO_4F \rightleftharpoons Na_{1.5}FePO_4F$. The second anodic and cathodic peaks at 3.02 V and 3.14 V, respectively, correspond to the second reversible phase transformation of $Na_{1.5}FePO_4F \rightleftharpoons NaFePO_4F$ of the Fe^{2+}/Fe^{3+} couple. These results are in good agreement with the galvanostatic charge-discharge cycling shown in **Fig. 8**.

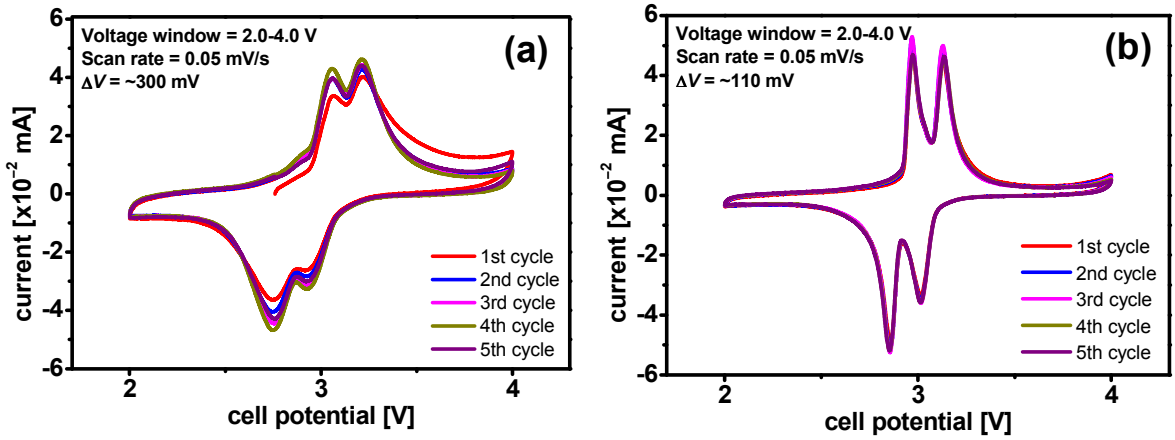

Fig. 11 Cyclic voltammogram for the (a) pristine; and (b) HEBM samples.

Furthermore, under similar electrode preparation and measurement conditions, the electrode made of the HEBM sample repeatedly shows less voltage polarisation (~110 mV) than the pristine one (~300 mV) as inferred from the peak positions of the cyclic voltammogram (see **Fig. 11**), indicating an enhanced electrochemical kinetics of HEBM sample. In addition, the HEBM electrode demonstrates good electrochemical reversibility, as there is no significant change in the position of both the anodic and cathodic peaks upon cycling (only few cycles are shown for clarity purpose).

Redox reaction during cycling

Ex-situ XPS analysis was performed on HEBM electrode to investigate the transition of the Fe^{2+}/Fe^{3+} redox couple during the course of cycling. The phase transformation of $Na_2FePO_4F \rightarrow NaFePO_4F$ is expected during charging and back transformation of $NaFePO_4F \rightarrow Na_2FePO_4F$ during discharging, which is supplemented by the oxidation of iron from +2 to +3, and reduction from +3

to +2. The oxidation state of iron is probed using XPS data obtained on electrode at OCV, fully charged (to 4.0 V) and fully discharged (to 2.0 V) states. From **Fig. 12**, it is found that the fresh electrode has a binding energy (BE) peak located at 711.2 eV. This peak corresponds to the BE of Fe^{2+}. There is no Fe^{3+} species detected. During charging, which corresponds to Na^{+} extraction, the iron species experiences an oxidation transition from Fe^{2+} to Fe^{3+}. Accordingly, the Fe BE peak shifts to 712.2 eV, which corresponds to the BE of Fe^{3+}.[28-30] Upon a full discharge, all Fe^{3+} species are fully reduced to Fe^{2+}. From the above observations we can conclude that the insertion-extraction mechanism involves one mole of Na^{+}, which accounts for the high discharge capacity achieved in HEBM sample. *Ex-situ* XPS analysis was also performed on sodium, Na^{+}; phosphorous, P^{5+}; and oxygen, O^{2-} ions. As these ions do not exhibit multiple oxidation states, they demonstrated a constant BE throughout the OCV, charge and discharge states, as shown in **Fig. S3**.

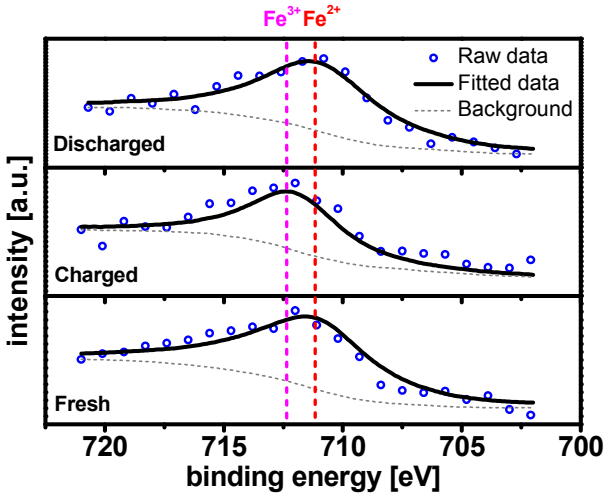

Fig. 12 *Ex-situ* XPS spectra of Fe^{2+}/Fe^{3+} redox couple obtained on a fresh, charged and discharged electrode.

Diffusion study

Cyclic voltammetry was recorded at different scan rates of 0.1 to 0.5 mV s^{-1} in a potential range of 2.0 to 4.0 V (**Fig. 13a**). As the scan rate increases, the height and the area of the CV curves increases, due to the constant capacity of the electrode (the ratio of the peak area and the scan rate yields the capacity). The peak current ratio of the anodic and cathodic peaks appear to be unity,[31] which indicates that there are no perceivable side reactions during the sodium insertion and extraction processes.[19, 28] The linear relationship between the peak current and the square root of the scan rate in **Fig. 13b** and **Fig. 13c** implies that the electrochemical process is solely controlled by diffusion,[19, 28, 31] which is a typical equilibrium behavior of an intercalation-type compound.

Electrochemical impedance spectroscopy (EIS) measurement was performed on a fresh three electrode cell at open-circuit voltage (OCV) for both the pristine and HEBM samples. The obtained experimental data as shown in **Fig. 14a** were fitted using the equivalent circuit model (**Fig. 14b**), which constitutes R_s at high frequency, two resistances, R_1 and R_2 along with constant phase elements, CPE_1 and CPE_2 at high and medium frequency regions respectively and a Warburg impedance, Z_w. While the intercept at the Z_{re} axis in the high frequency range (R_s) corresponds to the electrolyte, the high-frequency semicircle (R_1) is attributed to the Na ion transfer resistance through the passivation layer, whereas the medium-frequency semicircle (R_2) refers to the charge transfer resistance for the electrons and Na ions [27, 32] across the electrode-electrolyte interface, carbon-particle interface and particle-particle contact.[33] The inclined slope observed in the low frequency range is attributed to the Warburg impedance, Z_w, which corresponds to Na chemical diffusion (ambipolar diffusion which comprise of motion of Na ion along with electron) in the bulk of the electrode. The fitted values of R_s, R_1 and R_2 are presented in **Table 4**. The relatively smaller R_1 value for the HEBM sample implies less Na ion transfer resistance at the solid-electrolyte interface.[34] The smaller R_2 of the HEBM sample also means a faster charge transfer at various interfaces present compared to those in pristine sample.[28]

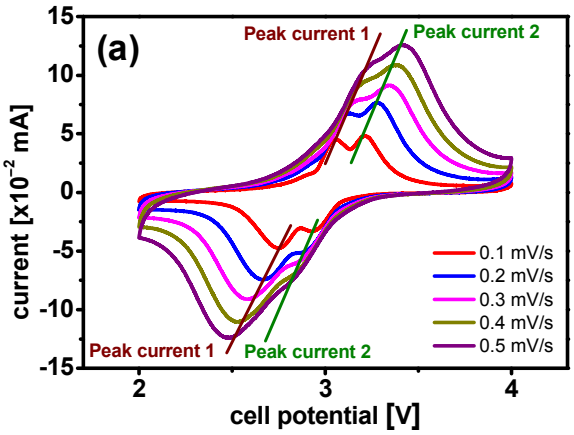

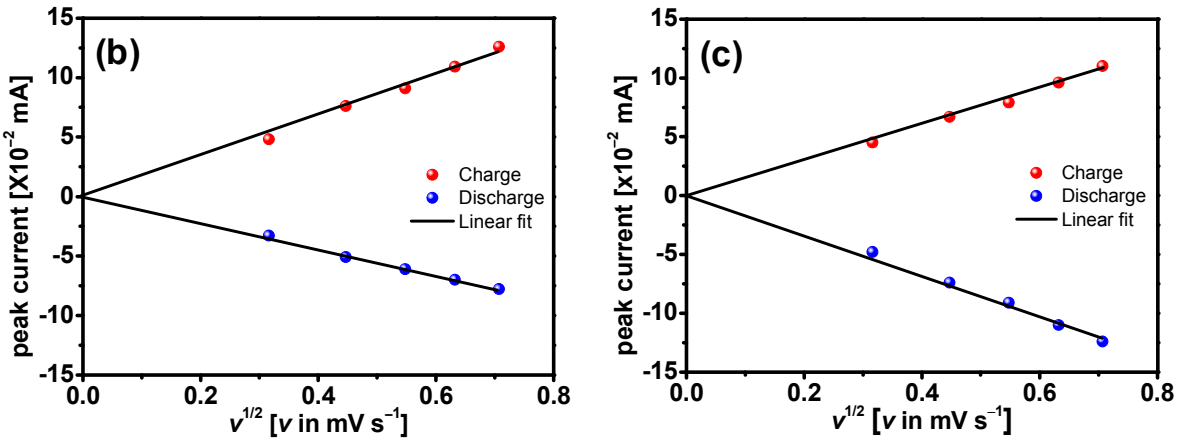

Fig. 13 (a) Cyclic voltammogram for the HEBM sample at different scan rates of 0.1, 0.2, 0.3, 0.4 and 0.5 mV s−1. The relationship between the peak current and the square root of the scan rate for (b) peak current 1; and (c) peak current 2.

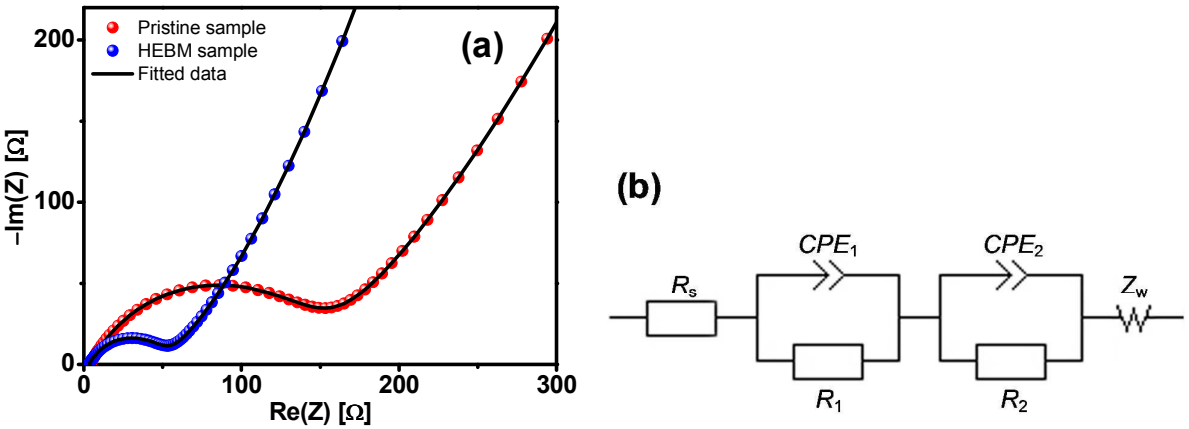

Fig. 14 (a) Nyquist plots of the electrochemical impedance spectra of pristine and HEBM Na2FePO4F sample obtained from fresh cell at OCV, and (b) equivalent circuit.

Table 4 Impedance parameters obtained using an equivalent circuit model.

Electrode material	R_s (Ω)	R_1 (Ω)	R_2 (Ω)
Pristine	3.96	63.11	47.26
HEBM	3.08	16.93	27.69

a Footnote text.

EIS is a technique which has been established as a reliable method to calculate the lithium and sodium chemical diffusion coefficient of the intercalation-deintercalation compounds.[35-37] The respective Na chemical diffusion coefficient of the pristine and HEBM samples can be calculated using the following equation:[38-40]

$$D_{Na} = \frac{R^2T^2}{2A^2n^4F^4C^2\sigma^2} \quad (1)$$

Herein, D_{Na} is the Na chemical diffusion coefficient ($cm^2\ s^{-1}$), R is the ideal gas constant (8.314 J mol^{-1} K^{-1}), T is the ambient temperature in absolute term (303.15 K), A is the contact area of the electrode (2.01 cm^2), n is the number of electrons per molecule during oxidisation, F is the Faraday constant (96,486 C mol^{-1}), C is the concentration of Na^+ (3.80×10^{-3} mol cm^{-1}), and σ is the Warburg coefficient ($\Omega\ s^{-1/2}$).

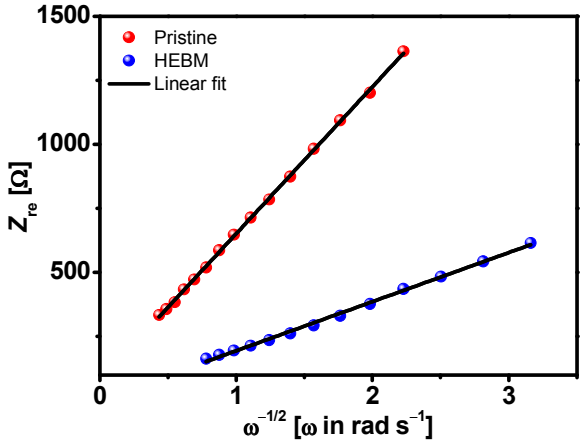

Fig. 15 Linear fittings between Z_{re} and $\omega^{-1/2}$ in the low frequency region.

Table 5 Warburg coefficient and calculated Na diffusion coefficient.

Electrode material	Warburg coefficient, σ ($\Omega\ s^{-1/2}$)	D_{Na} ($cm^2\ s^{-1}$)
Pristine	573.91	8.54×10^{-15}
HEBM	191.62	7.66×10^{-14}

a Footnote text.

The Warburg coefficient, σ, is associated with Z_{re} based on the following equation:[41]

$$Z_{re} = R_s + R_{ct} + \sigma\omega^{-1/2} \quad (2)$$

where ω is the angular frequency. From Equation (2), the Warburg coefficient, σ, can be determined from the gradient of the Z_{re} vs. $\omega^{-1/2}$ plot. **Fig. 15** shows the linear relationship between Z_{re} and the reciprocal square root of the angular frequency, $\omega^{-1/2}$ at low frequency region. By using Equation (1) the calculated Na chemical diffusion coefficient for both the samples are tabulated in **Table 5**. It is interesting to note that the calculated diffusion coefficient for the HEBM sample is one order of magnitude higher than the pristine sample.

The relatively low antisite disorder upon HEBM followed by post-heat treatment results in a more favourable Na migration along different possible channels in this 2D layered Na_2FePO_4F, showing one order of magnitude higher sodium chemical diffusion coefficient compared to the pristine sample. The lower antisite disorder in the HEBM sample in turn results in an enhanced sodium storage performance compared to the pristine sample, as well as impressive long-term cyclability. The enhanced Na diffusion along with reduced impedances for the charge transfer and sodium ion transport across various interfaces reduces the ohmic polarisation observed in this study for the HEBM sample. It is thus believed that the low antisite disorder in the HEBM sample promotes a more kinetically facile diffusion property, demonstrating an enhanced sodium storage performance compared to the pristine sample.

Conclusions

In summary, we report sodium storage performance of Na_2FePO_4F prepared via a soft template method, followed by high-energy ball milling and post-heat treatment. The HEBM sample delivered a discharge capacity of 116 and 78 mAh g^{-1}, at 0.1 C and 1 C, respectively while pristine sample without the HEBM process demonstrated a relatively low sodium storage performance of 87 mAh g^{-1} at 0.1 C. The HEBM sample exhibited stable cycling performance up to 200 cycles at 1 C, retaining almost 80% of its initial capacity, with an average coulombic efficiency of 99.4%. The possible reasons for the enhanced sodium storage performance of the HEBM sample compared to the pristine sample are discussed in terms of its relatively (i) small particle size; (ii) high surface area; (iii) low antisite disorder concentration; and (iv) enhanced transport properties.

Acknowledgement

Markas would like to thank NUS, Singapore for research scholarship. PB thanks NUS for funding sodium battery research. Authors thank Srirama Hariharan for critical review of this manuscript. Insightful discussions with Sunil Kumar and Mangayarkarasi Nagarathinam are gratefully acknowledged.

a Department of Mechanical Engineering, National University of Singapore, 9 Engineering Drive 1, Singapore 117576
**Corresponding author. Tel: +65 6516 7644; Fax: +65 6779 1459. Email: mpepb@nus.edu.sg.*

References

1. Y. Zhu, Y. Xu, Y. Liu, C. Luo and C. Wang, Nanoscale, 2013, 5, 780-787.
2. B. L. Ellis and L. F. Nazar, Current Opinion in Solid State and Materials Science, 2012, 16, 168-177.
3. V. Palomares, P. Serras, I. Villaluenga, K. B. Hueso, J. Carretero-Gonzalez and T. Rojo, Energy & Environmental Science, 2013, 5, 5884-5901.
4. S. Y. Hong, Y. Kim, Y. Park, A. Choi, N.-S. Choi and K. T. Lee, Energy & Environmental Science, 2013, 6, 2067-2081.
5. S.-W. Kim, D.-H. Seo, X. Ma, G. Ceder and K. Kang, Advanced Energy Material, 2012, 2, 710-721.
6. X. Wu, J. Zheng, Z. Gong and Y. Yang, Journal of Materials Chemistry, 2011, 21, 18630-18637.
7. Y. Kawabe, N. Yabuuchi, M. Kajiyama, N. Fukuhara, T. Inamasu, R. Okuyama, I. Nakai and S. Komaba, Electrochemistry, 2012, 80, 80-84.
8. B. L. Ellis, W. R. M. Makahnouk, Y. Makimura, K. Toghill and L. F. Nazar, Nature Materials, 2007, 6, 749-753.
9. N. Recham, J.-N. Chotard, L. Dupont, K. Djellab, M. Armand and J.-M. Tarasconz, Journal of The Electrochemical Society, 2009, 156, A993-A999.
10. Y. Kawabe, N. Yabuuchi, M. Kajiyama, N. Fukuhara, T. Inamasu, R. Okuyama, I. Nakai and S. Komaba, Electrochemistry Communications, 2011, 13, 1225-1228.
11. A. Langrock, Y. Xu, Y. Liu, S. Ehrman, A. Manivannan and C. Wang, Journal of Power Sources, 2013, 223, 62-67.
12. V. Ramar and P. Balaya, Physical Chemistry Chemical Physics, 2013.
13. N. Yabuuchi, M. Sugano, Y. Yamakawa, I. Nakai, K. Sakamoto, H. Muramatsu and S. Komaba, Journal of Materials Chemistry, 2011, 21, 10035-10041.
14. P. P. Prosini, P. Gislon, C. Cento, M. Carewska and A. Masci, Materials Research Bulletin, 2013, 48, 3438-3448.
15. B. L. Ellis, W. R. M. Makahnouk, W. N. Rowan-Weetaluktuk, D. H. Ryan and L. F. Nazar, Chemistry of Materials, 2010, 22, 1059-1070.
16. R. Tripathi, S. M. Wood, M. S. Islam and L. F. Nazar, Energy & Environmental Science, 2013, 6, 2257-2264.
17. G. F. Zhou, M. J. Zwanenburg and H. Bakker, Journal of Applied Physics, 1995, 78, 3438-3444.
18. S.-P. Badi, M. Wagemaker, B. L. Ellis, D. P. Singh, W. J. H. Borghols, W. H. Kan, D. H. Ryan, F. M. Mulder and L. F. Nazar, Journal of Materials Chemistry, 2011, 21, 10085-10093.
19. V. Ramar, K. Saravanan, S. R. Gajjela, S. Hariharan and P. Balaya, Electrochimica Acta, 2013, 105, 496-505.
20. K. S. W. Sing, D. H. Everett, R. A. W. Haul, L. Moscou, R. A. Pierotti, J. Rouquerol and T. Siemieniewska, Pure and Applied Chemistry, 1985, 57, 603-619.
21. J. Chen and J. Graetz, Applied Materials & Interfaces, 2011, 3, 1380-1384.
22. D. Morgan, A. V. d. Ven and G. Ceder, Electrochemical and Solid-State Letters, 2004, 7, A30-A32.
23. B. H. Toby, Powder Diffraction, 2006, 21, 67-70.
24. H. Fang, Z. Pan, L. Li, Y. Yang, G. Yan, G. Li and S. Wei, Electrochemistry Communications, 2008, 10, 1071-1073.
25. S. Yang, Y. Song, P. Y. Zavalij and M. S. Whittingham, Electrochemistry Communications, 2002, 4, 239-244.
26. J. Chen and M. S. Whittingham, Electrochemistry Communications, 2006, 8, 855-858.
27. A. Rudola, D. Aurbach and P. Balaya, Electrochemistry Communications, 2014, 46, 56-59.
28. V. Ramar and P. Balaya, Physical Chemistry Chemical Physics, 2013, 15, 17240-17249.
29. V. P. Zakaznova-Herzog, H. W. Nesbitt, G. M. Bancroft and J. S. Tse, Surface Science, 2006, 600, 3175-3186.
30. H. Yang, X.-L. Wu, M.-H. Cao and Y.-G. Guo, Journal of Physical Chemistry C, 2009, 113, 3345-3351.
31. L. Li, X. Tang, H. Liu, Y. Qu and Z. Lu, Electrochimica Acta, 2010, 56, 995-999.
32. D. Aurbach, Journal of Power Sources, 2000, 89, 206-218.
33. Y.-M. Choi and S.-I. Pyun, Solid State Ionics, 1997, 99, 173-183.
34. J. Dou, X. Kang, T. Wumaier, N. Hua, Y. Han and G. Xu, Journal of Solid State Electrochemistry, 2012, 16, 1925-1931.
35. N. Böckenfeld and A. Balducci, Journal of Solid State Electrochemistry, 2014, 18, 959-964.
36. X. H. Rui, N. Ding, J. Liu, C. Li and C. H. Chen, Electrochimica Acta, 2010, 55, 2384-2390.
37. P. P. Prosini, M. Lisi, D. Zane and M. Pasquali, Solid State Ionics, 2002, 148, 45-51.
38. F. Gao and Z. Tang, Electrochimica Acta, 2008, 53, 5071-5075.
39. X. Fang, J. Li, K. Huang, S. Liu, C. Huang, S. Zhuang and J. Zhang, Journal of Solid State Electrochemistry, 2012, 16, 767-773.
40. B. Jina, E. M. Jin, K.-H. Park and H.-B. Gu, Electrochemistry Communications, 2008, 10, 1537-1540.
41. K. Yang, Z. Deng and J. Suo, Journal of Solid State Electrochemistry, 2012, 16, 2805-2813.